

# Radiation pressure-tunable photoluminescence and upconversion lasing on a chip

Christiaan J. Bekker,\* Christopher G. Baker, and Warwick P. Bowen

*School of Mathematics and Physics*

*The University of Queensland, Brisbane, Australia 4072*

(Dated: May 18, 2022)

The ability to tune the wavelength of light emission on a silicon chip is important for scalable photonic networks, distributed photonic sensor networks and next generation computer architectures. Here we demonstrate light emission in a chip-scale optomechanical device, with wide tunability provided by radiation pressure. To achieve this, we develop an optically active double-disk optomechanical system through implantation of erbium ions. We observe radiation pressure tuning of photoluminescence in the telecommunications band with a wavelength range of 520 nm, green upconversion lasing with a threshold of  $340 \pm 70 \mu\text{W}$ , and optomechanical self-pulsing caused by the interplay of radiation pressure and thermal effects. These results provide a path towards widely-tunable micron-scale lasers for photonic networks.

## I. INTRODUCTION

Active microcavities are a promising technology for the development of on-chip light sources for integrated photonic networks. The addition of a gain medium to a microcavity allows redistribution of power between optical modes and the ability to generate lasing in the cavity through population inversion. The strong optical confinement and small mode volumes of whispering gallery mode (WGM) systems in particular are useful in applications that require large photonic networks with multiplexing and many components [1, 2]. WGM cavities have been demonstrated as on-chip laser light sources [3] and stabilisation elements for external laser pumps [4]. A variety of active WGM geometries exist, with gain media introduced through active sol-gel [4–8] or silicon-rich oxide [9] coatings, rare-earth ion implantation [10–13] or doping [14–16], embedded quantum wells [3, 17, 18] and fluorescent dyes [19–21]. However current demonstrations of active WGM systems have a fixed emission frequency set by the device geometry or are dynamically swept through mechanical self-oscillation [18]. Furthermore imperfect fabrication tolerances, particularly significant for reflow microtoroids [22], make it difficult to interface multiple devices in a network [23].

In this work, we demonstrate the first active double-disk optomechanical system, using implanted erbium ions as the gain medium. The very large optomechanical interaction between the disks provides a degree of control to tune the photoluminescence from the cavity. Combined with the high mechanical compliance of the double-disk geometry, this allows a radiation pressure-driven tuning range of nearly 7% of the device free spectral range (FSR), which is demonstrated in the telecommunications band. Furthermore, green ( $\sim 550 \text{ nm}$ ) upconversion lasing with a threshold of  $340 \pm 70 \mu\text{W}$  is demonstrated for the first time in a double-disk geometry, and arises as a natural characteristic of the implanted erbium used

as a gain medium [24]. The lasing frequency is tunable by the same mechanism as the telecom photoluminescence. Our results provide a pathway towards widely tunable lasers for photonic circuits, with applications such as distributed and precision photonic sensors [25–28], and photonic buses in next generation computer architectures [1, 29].

## II. ACTIVE DOUBLE-DISK RESONATOR

While less widespread than microtoroids or microdisks, double-disk optomechanical systems have been developed by several groups using silica [23, 33–35] and silicon nitride [36–38], with more recent implementations in silicon carbide [39], lithium niobate [40, 41] and double-layer silicon-on-insulator [42]. The geometry consist of two disk cavities stacked vertically such that the evanescent fields of the disks overlap. This causes the optical modes to hybridise into ‘supermodes’ existing in both disks, with a significant proportion of the mode residing in the gap between the disks (See insets of Fig. 1(c)). This causes the effective refractive indices  $n_{\text{eff}}$  of the optical modes to be extremely sensitive to the size of the gap.

The resonance condition for WGM optical cavities is given by:

$$2\pi R n_{\text{eff}} = m \lambda_{0,m} \quad (1)$$

where  $R$  denotes the radius of the device,  $m$  the azimuthal mode number and  $\lambda_{0,m}$  the resonance wavelength of the cavity for a given mode number. Therefore, as the effective refractive index of the modes are changed with changing disk spacing  $x$ , the resonance frequencies of the cavity  $\omega_{0,m} = \frac{2\pi c}{\lambda_{0,m}}$  are accordingly shifted. This provides double-disk systems with a very large optomechanical coupling strength, namely  $G = \partial\omega_{0,m}/\partial x \sim 10 \text{ GHz/nm}$  [23] which is to first order dependent on the disks’ thickness and vertical (out-of-plane) separation instead of the radius  $R$  of the device [23], as is the case

\* c.bekker@uq.edu.au

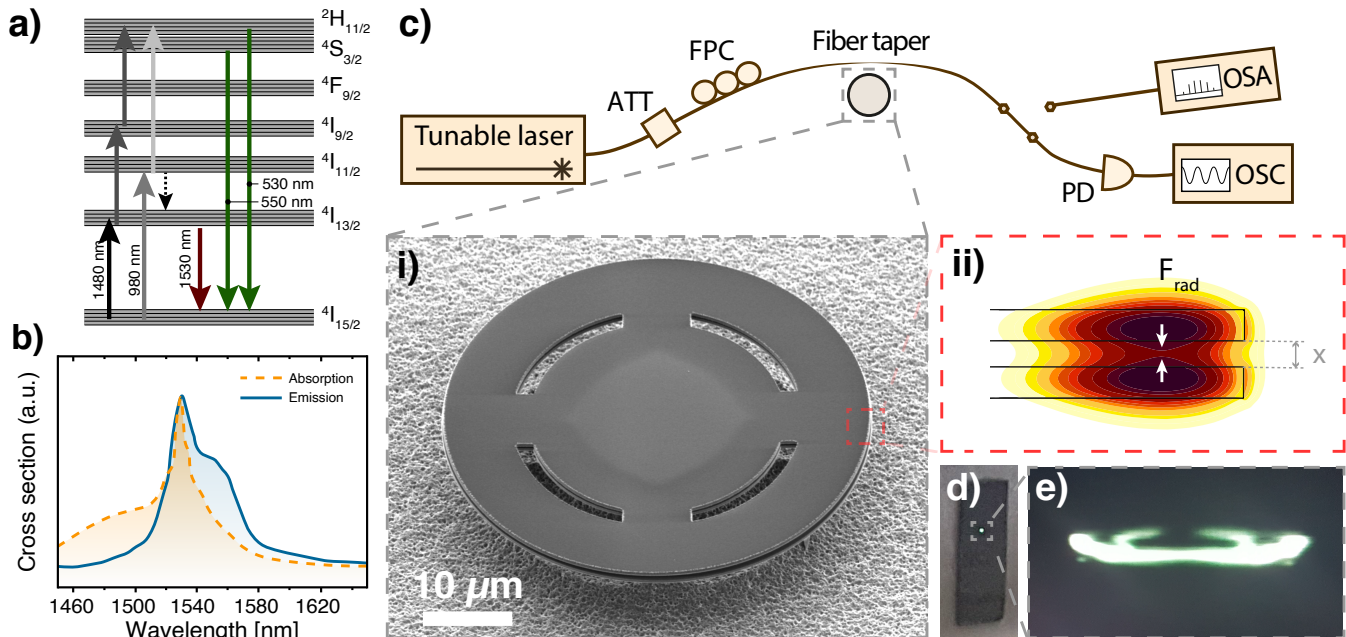


FIG. 1. (a) Energy levels of erbium implanted in a silica matrix [30, 31]. Each level is broadened through the Stark effect. Common pumping (left) and emission (right) pathways are denoted by arrows, including multi-photon and non-radiative relaxation (dashed) processes. (b) Absorption and emission cross-sections for erbium at telecommunications wavelengths in a silica matrix. Adapted from data in Ref. [32]. (c) Schematic of the experimental setup. ATT: Attenuator, FPC: Fibre Polarization Controller, PD: Photodetector, OSA: Optical Spectrum Analyzer and OSC: Oscilloscope. Insets: i) SEM image of an erbium-doped slotted double-disk device. ii) COMSOL Multiphysics simulation of the fundamental bonding optical WGM, color denotes intensity of electromagnetic field. The frequency of the mode is sensitive to displacements which change the air gap  $x$  between the disks, and tuning is accomplished through the radiation pressure force  $F_{rad}$ . (d) Photograph of green emission from device visible with the naked eye. (e) Microscope camera side-view of device emitting green light.

in single disk resonators where  $G \sim \omega/R$  [43]. This allows the resonance frequency of the WGM modes to be widely tuned with extremely weak forces, such as radiation pressure [35, 38] and capacitive actuation through the use of integrated interdigitated electrodes [23], and for the fabrication of larger devices to increase mechanical compliance without degrading the optomechanical coupling strength. These characteristics are rare among WGM systems, and make double-disk cavities strong candidates for use as on-chip tunable light sources.

### A. Erbium luminescence pathways

The rare-earth element erbium is often used as a gain medium for lasing due to its natural operation in the telecommunications frequency band ( $\lambda \sim 1550$  nm). Figure 1(a) shows the energy levels of erbium in a silica matrix. Each level is split into a manifold due to the Stark effect [44], so that the absorption spectrum of the erbium consists of bands with broad absorption ranges. For emission in the telecommunications band ( $\lambda \sim 1550$  nm), Fig. 1(b) shows the absorption and emission cross-sections of erbium ions in silica [32]. The main driving pathway is typically to excite ions to the upper states

in the  $4I_{15/2}$  band with a laser of wavelength around 1480 nm. The ions decay non-radiatively to the lowest state in the band, and emit a photon of approximately 1530 nm wavelength to return to the ground state. Alternatively, a 980 nm pump source can be used to excite ions to the  $4I_{11/2}$  band, as they spontaneously decay from there to the  $4I_{15/2}$  band [8].

In addition to the driving mechanisms above, absorption of multiple pump photons can excite the erbium to the  $2H_{11/2}$  or  $4S_{3/2}$  bands, with relaxation to the ground state accompanied by the emission of an upconverted green photon ( $\lambda = 550$  nm or 530 nm).

### B. Device design and fabrication

The active double-disks implemented here are  $50 \mu\text{m}$  in diameter and designed with a slot and four tethers to support the outer annulus, as shown in Fig. 1(c)(i). The slot is included to reduce warping of the disks due to internal material stress gradients [23] and to allow greater under-etching of the disks.

The fabrication process for these devices is similar to that presented in Ref. [23], with the addition of an erbium implantation step. A  $\text{SiO}_2/\alpha\text{-Si}/\text{SiO}_2$  stack with

nominal thickness 350/300/350 nm is deposited on a crystalline Si substrate using PECVD. The top disk is subsequently implanted with erbium ions using a 1.7 MV tandem Pelletron<sup>®</sup> accelerator, with a total ion fluence of  $4 \times 10^{15}$  ions/cm<sup>2</sup>. The chip is annealed to repair implantation damage at a temperature of 900°C for a period of five hours (See Appendix A for discussion of the annealing process). The double-disk stack is defined through electron-beam lithography with ma-N 2410 negative resist (Micro Resist technology GmbH.) and three successive reactive ion dry-etching steps. Each layer is etched using an optimised etch chemistry consisting of SF<sub>6</sub>, CHF<sub>3</sub> and CF<sub>4</sub> gases. After removal of the resist with an oxygen plasma process the silicon substrate and amorphous silicon sacrificial layer are released with an isotropic xenon difluoride dry etch.

### C. Measurement Setup

A schematic of the experimental setup is shown in Fig. 1(c). Optical spectroscopy is performed using a tunable continuous wave diode laser (Yenista T100S-HP) in the 1500-1600 nm wavelength band. Input light is coupled into the double-disk through a tapered optical fiber, and the transmitted optical intensity is detected on a high-speed photodetector. Optical quality factors on the order  $10^5$  are typically observed in these devices, similar to the values observed in other silica double-disk optomechanical systems [23, 35]. Alternatively, the transmitted light can be analyzed on an optical spectrum analyzer (OSA) to detect photoluminescence from the implanted erbium.

While driving at 1480 nm is optimal due to the small emission cross-section of the ions [12] as shown in Fig. 1(b), effective excitation can be achieved up to a wavelength of  $\sim 1510$  nm. This allows driving of the device in our experiments using an optical resonance situated around 1506 nm. The resulting photoluminescence is strongest around 1535 nm, and drops off for wavelengths below 1500 nm and above 1570 nm. Section III outlines the experimental observation of photoluminescence in the 1550 nm band in our device.

We additionally observe significant green emission from our devices while pumping in the telecommunication band, both with the naked eye (Fig. 1(d)) and with an optical microscope camera (Fig. 1(e)). This green emission was not guided in the optical fiber used to pump the cavity, but could be captured with a CCD microscope camera in order to extract the intensity of the emission and reveal upconversion lasing [5], as discussed in Section IV.

### III. PHOTOLUMINESCENCE AT TELECOMMUNICATION FREQUENCIES

When erbium ions are implanted in a WGM cavity and the system is pumped in a region of strong erbium ab-

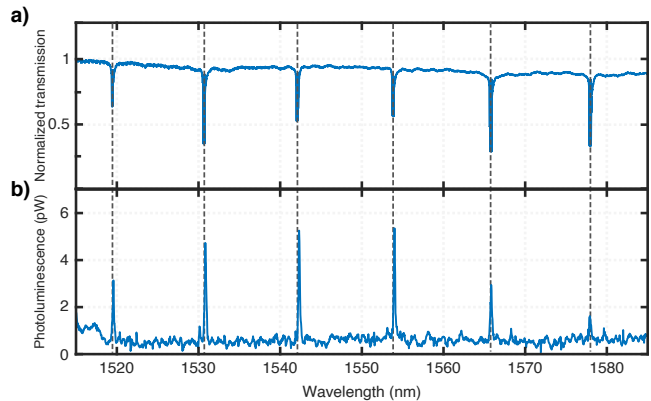


FIG. 2. Comparison between optical mode spectrum and photoluminescence emission peaks in the near infrared band. a) Optical transmission spectrum showing a set of WGMs separated by the device FSR. b) OSA photoluminescence spectrum acquired while the cavity is pumped using a WGM mode at about 1506 nm showing emission peaks at wavelengths corresponding to device WGMs. The peaks are not visible above the noise floor outside of this band, confirming that the emission is indeed due to the implanted erbium.

sorption, Purcell enhancement [45] causes the photoluminescence from the ions to preferentially occur at frequencies corresponding to optical cavity modes in the emission region. Hence, when the cavity is optically pumped, spectrally narrow peaks separated by the FSR of the optical cavity are expected across the entire erbium emission range [12, 46]. Optical spectroscopy of the device is first performed by sweeping the frequency of the input laser and detecting the outcoupled light on a high-speed photodetector. This reveals the optical spectrum of the double-disk shown in Fig. 2(a), where one family of WGM modes is visible.

In order to detect photoluminescence from the erbium, the pump laser is detuned to the side of an undercoupled optical resonance of the double-disk with a wavelength of 1506.4 nm. The transmitted light is sent to an optical spectrum analyzer (OSA, Yokogawa AQ 6374), and the resulting peaks are plotted in Fig. 2(b).

Figure 2 confirms the expectation that photoluminescence from the erbium predominantly occurs at the WGM resonances of the double disk. The dashed vertical lines between the plots emphasise the shared frequency of each WGM resonance and emission peak. The comb of photoluminescence peaks extends over the range of 1520-1580 nm, as shown in Fig. 2(b), and drops below the level of the measurement noise outside of these bounds. This spectrum is consistent with what would be expected for optical emission from the erbium within the WGM cavity [5, 12, 46, 47].

### A. Photoluminescence tuning

Since the frequencies of the erbium photoluminescence emission peaks are directly linked to the device's WGM resonance frequencies, they can be directly controlled by tuning the optical modes. In Fig. 3, the emission from a mode at a nominal wavelength of 1540 nm is tuned over a wavelength range of 520 pm by detuning the pump laser positioned on the side of an optical resonance at about 1506 nm. While the thermo-optic effect and mechanical expansion from photothermal heating of the device play a role in the observed tuning, the dominant effect is based on radiation pressure where the optical gradient force between the double disks changes the size of the air gap (See Appendix B for calculations and discussion of the tuning mechanisms present in this system). As the laser is detuned closer to the cavity resonance frequency more optical power enters the cavity, increasing the mechanical deformation due to the optical gradient force and shifting the optical resonance frequency. This leads to the triangular mode shape in Fig. 3(a).

The photoluminescence tuning accompanying optical resonance frequency tuning is shown in Fig. 3(b), where a photoluminescence peak is tuned as the pumping laser frequency is varied. The central frequency of the photoluminescence peak indicates the tuned resonance frequency of the optical mode and the width of the peak its spectral shape. Optical resonance frequency tuning over a full FSR using radiation pressure has been demonstrated in similar devices [38], allowing photoluminescence at any arbitrary frequency within the material transparency window. Large tuning using capacitive actuation is also possible [23, 48], and can provide a mechanism to tune photoluminescence independently of the optical pump.

## IV. GREEN UPCONVERSION LASING

As the pump power is increased, we expect to see an increase in the photoluminescence intensity in the telecommunications band. However even at low input powers ( $\leq 1$  mW) saturation of the telecommunications band photoluminescence occurs, and we instead observe an increase in the emission of green light from the device arising from upconversion of the input light [5, 49]. Green light emission is visible from the device even with the naked eye, as shown in Fig. 1. The parameters of the fibre taper and optical fibre used in our experiment are chosen for guiding light in the telecommunications window. As such, the green emission is not guided and no signal could be detected on the OSA in this wavelength range. Instead, observation with a CCD microscope camera reveals that the emission is concentrated around the outer perimeter of the device, and as far as can be ascertained is emitted isotropically. Top-view images of the device are taken with the microscope camera (Fig. 4(a)), and post-processed to get a measure of the functional dependence of the intensity of the emission with pump

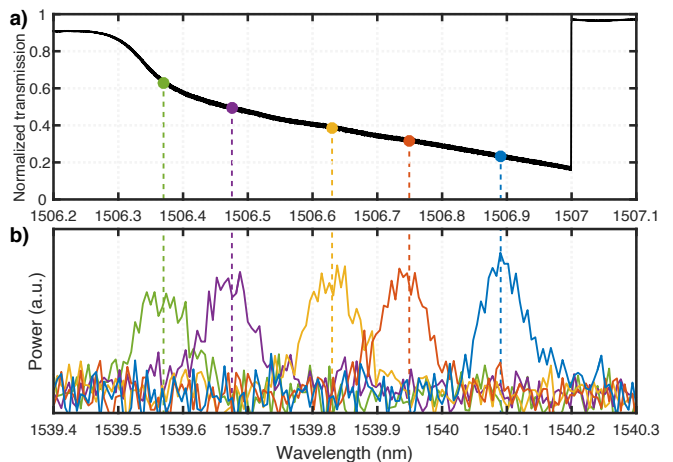


FIG. 3. Photoluminescence from the device as a function of the detuning of the pumping laser. a) Trace of an optical mode as the input laser is swept through it at a speed of 10 nm/s with a power of 10 mW. The triangular shape is characteristic of optomechanical pulling, and indicates the optical tuning range. Subsequently the laser was set to a constant detuning at each of the positions marked by a colored circle, and the optical emission was measured on an OSA. b) Resulting photoluminescence for each detuning of the input laser from a mode in the same family as the pumped mode. The luminescence peaks clearly demonstrate the photoluminescence frequency tuning, with peak shape indicating the equilibrium spectral shape of the mode. This radiation pressure-based tuning mechanism can span over several nm [38].

power.

To measure the intensity of the green emission, the software package ImageJ [50] is used to extract the intensity of pixels along a ring within the optical mode area in each image. This region is shown as a yellow dashed line in Fig. 4(a). The responsivity of the pixels in the CCD camera is a function of the frequency of the green emission. However, even at the maximum pump powers used in our experiments, the relative shift in the optical mode frequencies is less than 0.1%. Consequently, it is reasonable to approximate the responsivity as constant. The green component of the captured intensity saturates in the detector at input powers above 5 mW. Using the red component allows the intensity of the emission to be determined without reaching saturation (see Appendix C for further discussion).

In Fig. 4(b) the emitted intensity is plotted as a function of optical input power, yielding a clear linear trend. A least-squares fit gives the equation for the trendline  $I \propto (10.6 \pm 0.2)P_{\text{in}} - (3.6 \pm 0.8)$  mW where the uncertainties represent one standard deviation from the mean. This yields a threshold power of  $P_{\text{thresh}} = 340 \pm 70$   $\mu$ W. The existence of a threshold and linear dependence with pump power is consistent with green upconversion lasing [5]. Because the green light was not guided in the optical fibres used in the experimental setup, an optical spectrum of the lasing could not be obtained to deter-



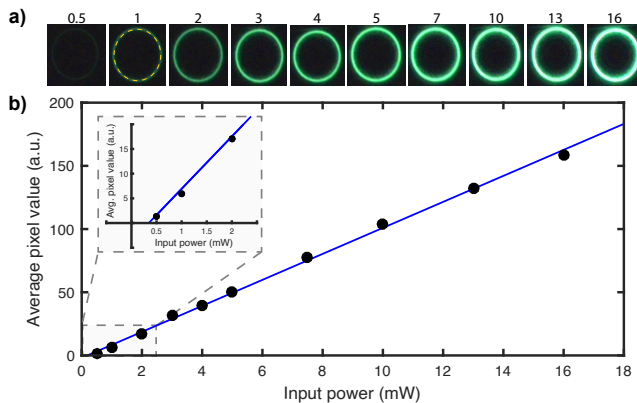


FIG. 4. Intensity of green optical emission as a function of input laser power, demonstrating green upconversion lasing. (a) Microscope images of emitting devices with increasing pump power. The region over which the optical intensity is recorded is denoted by a dashed yellow ring in the second image ('1'). (b) Photoluminescence intensity in the recorded region for each image, extracted using ImageJ. For this plot, the average of the red component in the RGB-intensity of the pixels in the recorded ring is measured, in order to avoid artefacts from the saturation of the camera present in the green component, see Appendix C. Assuming an approximately constant wavelength as a function of input power, this is directly proportional to the total intensity of the emitted light. Variations in recorded intensities between pixels were found to result in a less than 2% relative standard error in the total measured intensity. This is insignificant compared to the uncertainty in the pump power, which we believe accounts for the majority of the measurement uncertainty.

mine whether the lasing is single- or multimode.

To our knowledge this is the first demonstration of lasing in a double-disk optomechanical geometry. Furthermore, it is important to note that the tuning mechanism demonstrated in Fig. 3 applies to all of the cavity modes, giving confidence that the green lasing observed is also tunable. Further experiments could focus on suppressing green emission to produce lasing at telecommunications frequencies, or on capturing the green emission observed here in-fibre to directly observe tunable lasing.

### A. Concentration quenching

The presence of green upconversion lasing in our devices, as opposed to lasing in the telecommunications band, can be explained through concentration-quenching mechanisms, in particular cooperative upconversion and excited-state absorption (ESA) [51, 52]. Cooperative upconversion occurs between two neighboring excited erbium ions, where relaxation of one ion stimulates excitation of the other to a higher energy level [53], causing emission of a single higher-energy photon. ESA, on the other hand, occurs in a single ion as a two-step excitation process [31]. Both processes can be considered

concentration quenching, that is, effectively lowering the fraction of erbium in the first excited state at a given pump power [51] and therefore making lasing at telecommunication frequencies more difficult. This is especially the case for ESA, which can compete directly with stimulated emission if it occurs at the laser pumping frequency, effectively rendering lasing impossible in the 1550 nm band [52].

A further concentration quenching effect can arise from regions at the fringes of the optical mode, where the erbium ions are incompletely pumped. These regions give rise to a large absorption of pump power while not contributing to gain in the cavity, increasing the lasing threshold [11]. This effect can be avoided by selectively implanting regions of erbium where the optical modes will be situated through use of photoresist masks [54].

In order to achieve lasing at telecommunications frequencies, the effect of the material matrix on the erbium ions' energy levels must be carefully considered. For example, it has been demonstrated that cooperative upconversion can be reduced by optimising the homogeneity of the ion implantation process [31, 55].

## V. OPTOMECHANICAL INSTABILITY AND SELF-PULSING

In addition to the phenomena described up to this point, we observe self-pulsing optomechanical effects in our double-disk devices (Fig. 5). The existence of sets of forces acting with opposite magnitudes and on different characteristic timescales can lead to instabilities in the optomechanical resonator. Such instabilities have been reported in a variety of systems, where the thermo-optic effect in the cavity is opposed by free carrier dynamics [56], thermo-mechanical forces [7, 57, 58], gain dynamics in an external cavity [59] or the Kerr effect [60]. In each work a strong force with a short timescale pushes the resonator out of equilibrium, after which it slowly returns to its initial position through a force acting in the opposite direction. The large magnitude of the fast effect ensures that equilibrium is never attained. In our work, the fast driving is predominantly due to radiation pressure, while the slower relaxation is due to thermal effects. Both the radiation pressure and thermo-optic effects here increase the effective refractive index of the cavity, leading to a red-shift of the resonance, while the thermo-mechanical effect causes the disks to separate, blue-shifting the resonance. While the initial radiation-pressure 'kick' sends the mode off-resonance and eliminates further forcing from intracavity photons, the delayed thermal response of the cavity brings the mode back onto resonance [61]. Because the effects occur with different characteristic time constants, the steady state of the device is oscillatory, with the period of oscillation determined by the slow response.

The self-pulsing of the device can be controlled either through changing the detuning of the laser from optical

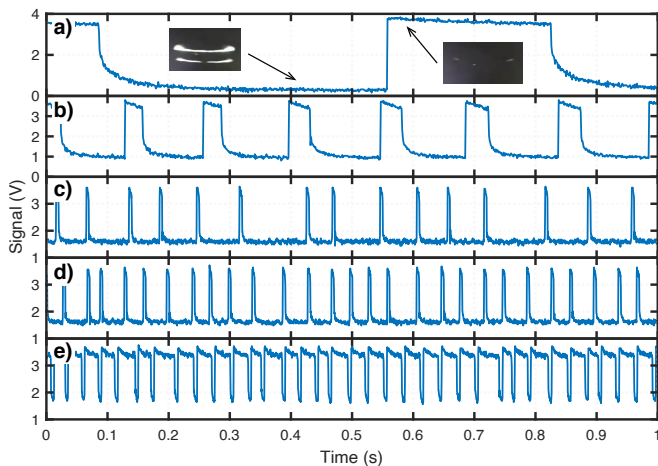


FIG. 5. Self-pulsing or ‘blinking’ of green photoluminescence in double-disk cavities under constant laser input. A large output signal means no coupling to the device, and corresponds to no light on the microscope camera, whereas when the signal dips to low values, the light is on resonance with the cavity and the device lights up with bright green emission (see insets in (a), including reflection from the substrate). The rate of blinking can be controlled (a-d) through changes in the pumping power and detuning from resonance - in general, a higher power and smaller detuning lead to slower blinking rates, as also observed in [57]. The style of the blinking can also be controlled in a similar manner, from rapid ‘dark’ blinks for a mostly lit device (d) to the case where the device rapidly blinks ‘on’ (e).

resonance or the coupling rate to the tapered fiber. Several experimental measurements with different laser detuning are shown in Fig. 5(a-e), corresponding to different periods and duty cycles. These are similar to the self-pulsing effects observed in other systems [7, 57, 62]. The observation of radiation pressure-dominated self-pulsing in these devices corroborates the radiation pressure-based tuning presented in Section III A.

It is important to note that this self-pulsing becomes much slower at higher optical powers due to mechanical stiffening of the device as the dropped power is increased [35], and the stronger thermal effects leading to an increased thermo-mechanical deformation. Indeed, stable coupling to the side of resonance is achievable with sufficient optical power (as is the case in Fig. 3). This strong optical spring effect due to blue-detuned optical driving is not accompanied here by mechanical instabilities (i.e. regenerative oscillation arising due to dynamical back-action [63]) due to the very high squeeze-film damping of the double-disk resonator’s vibrational modes in air [33, 35].

The combination of self-pulsing and a gain medium, in our case, allows the conversion of a continuous infrared pump into frequency-chirped pulsed signals, both as photoluminescence at infrared wavelengths and green lasing in the visible band. Self-pulsing behavior has been proposed as a method to sense fluctuations in humidity [62],

for biosensing [7] and for all-optical control and synchronization [59]. An interesting question for future work is whether the additional optomechanical dynamics and loss channels due to the intracavity gain medium introduced here interacts with the self-pulsing instability, creating new forms of self-pulsing dynamics (e.g. Ref. [18]).

## VI. CONCLUSION

In this work we have demonstrated radiation pressure-tunable photoluminescence in the telecommunications band and green upconversion lasing emitted from silica double-disk optomechanical systems. This is the first demonstration of optomechanical tuning of lasing and photoluminescence in an integrated WGM cavity, and the first demonstration of lasing in a double-disk cavity. The observation of radiation-pressure driven self-pulsing, the first in double-disks, provides the possibility to build pulsed light sources and explore new forms of optomechanical instability.

Engineering the energy levels of the implanted erbium should allow for low-threshold lasing to also be achieved at 1550 nm, leading to applications of the system as an optically pumped, micron-scale, integrated laser light source for ‘lab on a chip’ experiments or photonic integrated networks. Electronic tuning of the optical resonance frequencies can be achieved through capacitive actuation schemes, which has already been used to demonstrate super-FSR optical tuning ranges in similar devices [23], which opens up rich new capabilities for fully integrated photonic-electronic hybrid technologies [1].

## ACKNOWLEDGMENTS

The ion implantation for these devices was performed at the NCRIS facilities (ANFF and the Heavy Ion Accelerator Capability) at the Australian National University. Fabrication was performed at the Queensland node of the Australian National Fabrication Facility (ANFF-Q) and the Microscopy Australia Facility at the Centre for Microscopy and Microanalysis, The University of Queensland. The authors acknowledge these facilities and the scientific and technical assistance of the staff. The authors thank E. Cheng and G. Harris for valuable insights and discussions and M. Lyu for annealing the chips. This work is funded by the Australian Research Council Centre of Excellence in Engineered Quantum Systems (EQUS) (CE170100009) and the Commonwealth of Australia as represented by the Defense Science and Technology Group at the Department of Defense. C.J.B. and C.G.B. acknowledge support through an Australian Government Research Training Program (RTP) Scholarship and an Australian Research Council Fellowship (DE190100318), respectively.

## Appendix A: Device annealing

The first generation of devices were not annealed prior to fabrication. As shown in Fig. 6, the result was very large warping of the top silica disk. Even with just the tethers released (right-hand panel of Fig. 6), the warping is clearly visible. The reason for this is that during implantation, erbium ions dislocate other molecules from their places in the solid matrix both where the erbium is finally lodged and along its trajectory of travel. These dislocations cause not only large bulk stresses, but also a strong stress gradient in the material which enhances warping and distortion when the device is released. Here erbium was only implanted in the top disk, hence there was minimal damage to the bottom disk layer and consequently minimal warping as can be observed in Fig. 6.

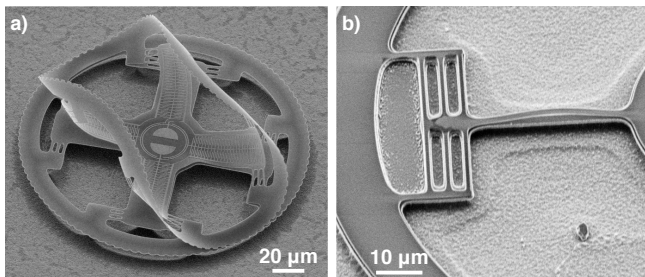


FIG. 6. Electron micrographs showing warping in unannealed devices with implanted erbium. This spectacular deformation arises from a stress gradient in the top disk induced by implantation damage, which must be repaired through an annealing step. The bottom disk had no implanted ions and displays minimal warping in comparison.

In order to negate this warping the chips are annealed after ion implantation and prior to any further processing being done. At temperatures above  $800^{\circ}\text{C}$ , the silica layers are allowed to relax, thereby ‘healing’ the dislocations from the erbium implantation process [13]. Though a few different parameters for annealing were used, it was found that sufficient layer repair is achieved by annealing at a temperature of  $800^{\circ}\text{C}$  for one hour in a muffle furnace (atmospheric environment). However, to maximise the relaxation from the process, annealing for most chips is done at  $900^{\circ}\text{C}$  for 5 hours. The inset of Figure 1(b) shows an SEM of a fabricated annealed device, where the stress from ion implantation has been successfully removed.

## Appendix B: Mechanism of optical resonance frequency tuning

Three forces interact in our system to tune the optical resonance frequencies of the device as a function of input

laser power. In this section we model these forces to assess the mechanism behind the tuning in Fig. 3.

Firstly, optical absorption in the silica of the disks causes heating and an increase of the material refractive index through the thermo-optic effect [64, 65]. This is further accompanied by thermal expansion of the heated material, which affects the spacing between the disks (this second effect is referred to here as the thermo-mechanical effect) and an opposing force due to mechanical rigidity. Lastly, optical power circulating in the cavity also alters the spacing between the disks through the radiation-pressure force.

The magnitude of the thermo-optic and thermo-mechanical effects can be estimated through use of finite element modelling. In Fig. 7(a), a COMSOL Multiphysics simulation of the thermal distribution in a slotted double-disk is shown. The tethers present a bottleneck to thermal dissipation, so that the temperature is mostly homogeneous in the outer annulus. This results primarily in in-plane expansion of the disks (which does not affect the disk separation), with out-of-plane deflection arising due to the differences in thermal expansion coefficients between Si and SiO<sub>2</sub> at the points where the top and bottom disks connect to the  $\alpha$ -Si sacrificial layer and Si pedestal, respectively.

While the intrinsic absorption of telecom photons in silica is very low, in practice the optical heating of the devices will be dominated by external parameters such as fabrication-induced defects or the presence of adsorbed water on the dielectric [66]. Hence the power dissipated as heat cannot be determined solely by analytical means. However, to investigate the potential of the thermo-optic and thermo-mechanical effects to act as the mechanism for tuning in this work, we take the limit where all power dissipated in the cavity is converted to heat. For this work, the injected power of the pump laser is set to  $P_{\text{in}} = 10$  mW. The contrast of the mode is 84% (or  $T = 0.16$ ) giving a maximum dropped power on resonance of  $P_d = 8.4$  mW. Therefore the largest amount of power dissipated as heat is  $P_{\text{heat}} = P_d = 8.4$  mW. The effective thermal resistance of the device was found from simulations to be  $R_{\theta} \simeq 10^5$  K/W, yielding a temperature change in the material of  $\Delta T_{\text{max}} = P_d R_{\theta} \simeq 840$  K. Note that this is an extremely large upper bound (demonstrated by the fact that, e.g., disks do not melt for  $P_d = 20$  mW, as they would in this limit) and Rayleigh scattering from surface roughness is likely the dominant loss mechanism for our cavity, given its  $Q \sim 10^5$  [65].

### 1. Thermo-optic effect

The thermo-optic coefficient of silica at room temperature is  $\frac{dn}{dT} \simeq 1 \times 10^{-5} \text{ K}^{-1}$  [67]. Therefore in the limit of all dropped power  $P_d$  being converted to heat, a refractive index change of the silica disks of  $\Delta n_{\text{SiO}_2} = \frac{dn}{dT} \Delta T_{\text{max}} = 8.4 \times 10^{-3}$  is expected. This does not directly correspond to a shift in the optical resonance

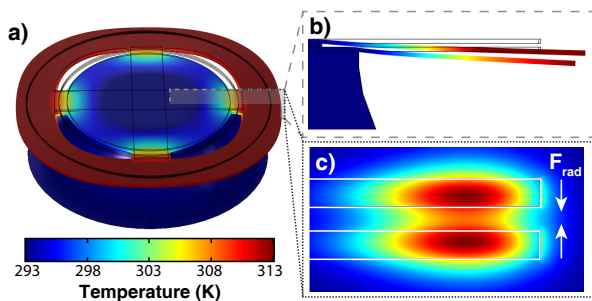


FIG. 7. (a) 3D-view and (b) side-view of a COMSOL Multiphysics simulation of thermal expansion in the slotted double-disk geometry in response to an applied temperature difference of 20 K between the disk perimeter and substrate, where the color scheme denotes temperature of the device in both cases. The thermal bottleneck in the system is at the anchor points, creating a thermal gradient which differentially displaces the disks in the vertical direction, corresponding to a shift in the optical resonance frequency. (c) Simulation of electromagnetic field strength (color) in a bonding optical whispering gallery mode hosted by the geometry, which imparts a vertical force on the disks due to radiation pressure.

through Eq. 1, since a proportion of the optical mode resides in the space between the disks, which does not experience a refractive index change. Instead, simulations provide a value for the shift of the optical resonance as a function of refractive index  $d\lambda/dn_{\text{SiO}_2} \simeq 160 \text{ nm}$ , [68] yielding an upper bound of the thermo-optic shift in the optical resonance of  $\Delta\lambda_{\text{TO}} = 1.34 \text{ nm}$ .

## 2. Thermo-mechanical effect

The thermal expansion of the double disks lead to a temperature-dependent change in the disk spacing, which in turn affects the effective refractive index of the optical mode. COMSOL simulations (see Fig. 7(b)) yield a value for the vertical displacement of the top disk relative to the bottom disk of  $dx/dT \sim 1.7 \times 10^{-3} \text{ nm/K}$ , or  $\Delta x = 1.4 \text{ nm}$  in the limit where all dropped power is converted to heat. This can be converted to a shift in the resonant frequency through  $\Delta\omega = G\Delta x$ , where  $G/2\pi \simeq 6.4 \text{ GHz/nm}$  [23] is the optomechanical coupling strength for an double-disk device with an air gap of 800 nm (obtained through COMSOL Multiphysics simulations, see Fig. 7(c)). The nominal size of the air gap is 350 nm, but a larger value is taken to account for stress-induced warping of the disks [23].  $\Delta x$  is the change in gap spacing, as defined earlier. Hence  $\Delta\omega = 2\pi \times 8.9 \text{ GHz}$ , or  $\Delta\lambda_{\text{TM}} = 0.07 \text{ nm}$ .

## 3. Radiation pressure force

The maximum frequency shift of the optical resonance frequency due to radiation pressure can be calculated us-

ing the equation  $\Delta\omega = G\Delta x$ , as defined earlier. From Hooke's law  $\Delta x = F_{\text{rad}}/k$ , where  $k$  is the effective spring constant of the double-disk system and the radiation pressure force  $F_{\text{rad}} = \hbar GN_{\text{cav}}$ . Finally we substitute the equation for the intracavity photon number  $N_{\text{cav}} = \frac{Q_i P_d}{\hbar\omega_0^2}$ , where  $Q_i$  denotes the intrinsic quality factor of the optical mode,  $\omega_0$  is the natural optomechanical resonance frequency and  $P_d$  is the power dropped into the cavity, as defined in previous sections. Therefore the equation for the maximal frequency shift due to radiation pressure becomes:

$$\Delta\omega = -\frac{Q_i G^2}{\omega_0^2 k} P_d \quad (\text{B1})$$

The spring constant is obtained via finite-element simulations (COMSOL), through applying a force  $F_{\text{rad}}$  to each disk (in opposite directions), and measuring the corresponding change in the spacing between the disks. Note that this measure for  $k$ , as opposed to the deformation in a single disk due to an applied force, is the origin of the factor of 2 difference between the equation presented here and that found in the literature [35, 38]. For out-of-plane bending, the simulations for this geometry yield  $k = 10 \text{ N/m}$ . Further we set  $Q_i \simeq 1 \times 10^5$  and  $\omega_0/2\pi = 1.947 \times 10^{14} \text{ Hz}$  to reflect a typical set of values from experiments. Therefore the predicted frequency tuning range through the radiation pressure force is  $\Delta\omega \simeq 86 \text{ GHz}$ . Alternatively, this can be expressed in terms of wavelength tuning as  $\Delta\lambda_{\text{RP}} \simeq 0.67 \text{ nm}$ .

## 4. Comparison of mechanisms

The effect of the thermo-optic and radiation-pressure effects on the optical resonance frequency ( $\Delta\lambda_{\text{TO}} \simeq 1.3 \text{ nm}$  and  $\Delta\lambda_{\text{RP}} \simeq 0.7 \text{ nm}$  respectively) are similar, and within the same order of magnitude as the observed optical tuning. However,  $\Delta\lambda_{\text{TO}}$  is derived as an extremely large upper bound and also does not account for stress-induced warping in the device, with the actual effect likely orders of magnitude weaker than this limit. As no such assumption was used for  $\Delta\lambda_{\text{RP}}$ , the radiation pressure-based tuning can be taken as dominant in this system. The predicted thermo-mechanical tuning mechanism is weaker than the other mechanisms by an order of magnitude, and can also safely be neglected.

While the predicted tuning range due to radiation pressure compares well with the observed tuning range of  $\sim 0.5 \text{ nm}$ , the size of the air gap is very uncertain in the system due to the effects of mechanical warping accrued during deposition of the dielectric stack or implantation of the erbium ions. A different air gap could alter the predicted optomechanical coupling strength of the device significantly, which has a large effect on the predicted tuning range since  $\Delta\omega \propto G^2$ . Note that a conservative value for the actual air gap between the disks in experiments was chosen, and stress engineering of the device



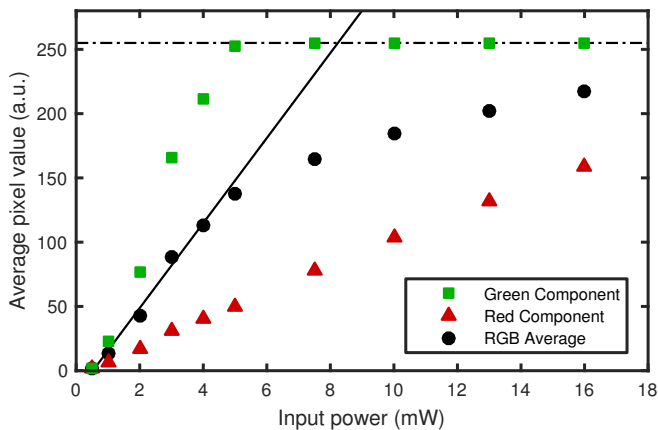


FIG. 8. Saturation of optical intensity measurements for green emission. The pixel value of the green component of the emission (green squares, measured using RGB color intensities) saturates at the maximum detectable value of 255 at an input power of 5 mW, indicated by a dash-dotted horizontal line in the figure. Correspondingly the total measured signal (black squares), which consists of a weighted average of red, green and blue components, deviates from its linear trend at this value, as clearly seen in the figure.

has the potential of increasing the radiation pressure-tuning range of these devices by an order of magnitude, if the nominal disk separation can be achieved [23].

### Appendix C: Saturation in the detection of green photoluminescence

In Section IV, green photoluminescence of the device resulting from multi-photon absorption in the implanted erbium is presented. The green emission is captured using an optical camera with a microscope objective to measure its dependence on the input power. The software package ImageJ is used to perform gamma correction on each image and to extract the individual R-, G-

and B-component values as well as the weighted intensity of each pixel in the brightest region of emission (which corresponds to the centre of the optical mode). This data is then used to extract an average value and standard deviation for each of the four parameters at different optical pump powers. In this section, we discuss these measurements, and justify the use of the red component to display the linear relationship between the green emission intensity and pump power in the main text.

For the same optical images shown in Fig. 4(a), Fig. 8 shows the weighted average of the RGB pixels corresponding to total intensity (black circles) and green component of the pixel RGB values (green squares). As can be seen in the Figure, the green pixel component grows rapidly with increasing input power, and saturates at the maximum pixel value of 255 (corresponding to the maximum signal measurable by the camera) at a power of 5 mW. Because the total intensity of the measured emission takes into account all three RGB components, a corresponding saturation and deviation from the linear trend is clearly observable for the black circles in Fig. 8 at pump powers larger than 5 mW. The fit to the first five points of the RGB average measurement (solid black line in Fig. 8) emphasises the linear trend before, and deviation after saturation.

Hence, neither the green component nor the RGB average measurements are accurate for input powers above 5 mW. In contrast, the red pixel measurement (red triangles in Fig. 8) does not approach saturation over the entire measured power range. This is because the wavelength of emission is in the green region of the visible spectrum, so that filtering out the ‘red’ component of the emission wavelength results in a strong attenuation of the signal. This does not imply that there is red light in the emission, but that the red pixels in the CCD camera have some responsivity at green wavelengths. Therefore we can have confidence in the results obtained for this component, as presented in Fig. 4(b), which indicates that the linear increase in the green emission intensity was maintained up to the highest pump power.

- 
- [1] A. H. Atabaki, S. Moazeni, F. Pavanello, H. Gevorgyan, J. Notaros, L. Alloatti, M. T. Wade, C. Sun, S. A. Kruger, H. Meng, K. A. Qubaisi, I. Wang, B. Zhang, A. Khilo, C. V. Baiocco, M. A. Popovi, V. M. Stojanovi, and R. J. Ram, *Nature* **556**, 349 (2018).
  - [2] A. W. Elshaari, I. E. Zadeh, A. Fognini, M. E. Reimer, D. Dalacu, P. J. Poole, V. Zwiller, and K. D. Jns, *Nature Communications* **8**, 379 (2017).
  - [3] M. Fujita and T. Baba, *Applied Physics Letters* **80**, 2051 (2002).
  - [4] L. Yang, D. K. Armani, and K. J. Vahala, *Applied Physics Letters* **83**, 825 (2003).
  - [5] T. Lu, L. Yang, R. V. A. van Loon, A. Polman, and K. J. Vahala, *Optics Letters* **34**, 482 (2009).
  - [6] S. Mehrabani and A. M. Armani, *Optics Letters* **38**, 4346 (2013).
  - [7] J. Park, S. K. Ozdemir, F. Monifi, T. Chadha, S. H. Huang, P. Biswas, and L. Yang, *Advanced Optical Materials* **2**, 711 (2014).
  - [8] Y. Yang, F. Lei, S. Kasumie, L. Xu, J. M. Ward, L. Yang, and S. N. Chormaic, *Optics Express* **25**, 1308 (2017).
  - [9] J. Verbert, F. Mazen, T. Charvolin, E. Picard, V. Calvo, P. No, J.-M. Grard, and E. Hadji, *Applied Physics Letters* **86**, 111117 (2005).
  - [10] A. Polman, B. Min, J. Kalkman, T. J. Kippenberg, and K. J. Vahala, *Applied Physics Letters* **84**, 1037 (2004).
  - [11] J. Kalkman, A. Polman, T. Kippenberg, K. Vahala, and M. L. Brongersma, *Nuclear Instruments and Methods in Physics Research Section B: Beam Interactions with Materials and Atoms* **242**, 182 (2006).
  - [12] T. J. Kippenberg, J. Kalkman, A. Polman, and K. J. Vahala, *Physical Review A* **74**, 051802 (2006).

- [13] B. Min, T. J. Kippenberg, L. Yang, K. J. Vahala, J. Kalkman, and A. Polman, *Physical Review A* **70** (2004).
- [14] V. Sandoghdar, F. Treussart, J. Hare, V. Lefvre-Seguin, J. M. Raimond, and S. Haroche, *Physical Review A* **54**, R1777 (1996).
- [15] W. von Klitzing, E. Jahier, R. Long, F. Lissillour, V. Lefvre-Seguin, J. Hare, J.-M. Raimond, and S. Haroche, *Journal of Optics B: Quantum and Semi-classical Optics* **2**, 204 (2000).
- [16] S. Zhu, L. Shi, B. Xiao, X. Zhang, and X. Fan, *ACS Photonics* **5**, 3794 (2018).
- [17] S. L. McCall, A. F. J. Levi, R. E. Slusher, S. J. Pearton, and R. A. Logan, *Applied Physics Letters* **APLCLASS2019**, 289 (1998).
- [18] D. Princepe, G. S. Wiederhecker, I. Favero, and N. C. Frateschi, *IEEE Photonics Journal* **10**, 1 (2018).
- [19] H.-B. Lin, A. L. Huston, B. L. Justus, and A. J. Campillo, *Optics Letters* **11**, 614 (1986).
- [20] M. Kuwata-Gonokami, R. H. Jordan, A. Dodabalapur, H. E. Katz, M. L. Schilling, R. E. Slusher, and S. Ozawa, *Optics Letters* **20**, 2093 (1995).
- [21] J. C. Knight, H. S. T. Driver, R. J. Hutcheon, and G. N. Robertson, *Optics Letters* **17**, 1280 (1992).
- [22] C. G. Baker, C. Bekker, D. L. McAuslan, E. Sheridan, and W. P. Bowen, *Optics Express* **24**, 20400 (2016).
- [23] C. Bekker, C. G. Baker, R. Kalra, H.-H. Cheng, B.-B. Li, V. Prakash, and W. P. Bowen, *Optics Express* **26**, 33649 (2018).
- [24] Z. Luo, Q. Ruan, M. Zhong, Y. Cheng, R. Yang, B. Xu, H. Xu, and Z. Cai, *Optics Letters* **41**, 2258 (2016).
- [25] M. Iqbal, M. A. Gleeson, B. Spaugh, F. Tybor, W. G. Gunn, M. Hochberg, T. Baehr-Jones, R. C. Bailey, and L. C. Gunn, *IEEE Journal of Selected Topics in Quantum Electronics* **16**, 654 (2010).
- [26] A. Washburn, W. Shia, K. Lenkeit, S.-H. Lee, and R. Bailey, *Analyst* **141**, 5358 (2016).
- [27] B. Stern, X. Ji, Y. Okawachi, A. L. Gaeta, and M. Lipson, *Nature* **562**, 401 (2018).
- [28] P. DelHaye, A. Schliesser, O. Arcizet, T. Wilken, R. Holzwarth, and T. J. Kippenberg, *Nature* **450**, 1214 (2007).
- [29] E. Kuramochi, K. Nozaki, A. Shinya, K. Takeda, T. Sato, S. Matsuo, H. Taniyama, H. Sumikura, and M. Notomi, *Nature Photonics* **8**, 474 (2014).
- [30] A. Polman, *Physica B: Condensed Matter* **300**, 78 (2001).
- [31] P. Kik and A. Polman, *MRS Bulletin* **23**, 48 (1998).
- [32] P. M. Becker, A. A. Olsson, and J. R. Simpson, *Erbium-Doped Fiber Amplifiers: Fundamentals and Technology* (Elsevier, 1999).
- [33] Q. Lin, J. Rosenberg, X. Jiang, K. J. Vahala, and O. Painter, *Physical Review Letters* **103**, 103601 (2009).
- [34] X. Jiang, Q. Lin, J. Rosenberg, K. Vahala, and O. Painter, *Optics Express* **17**, 20911 (2009).
- [35] J. Rosenberg, Q. Lin, and O. Painter, *Nature Photonics* **3**, 478 (2009).
- [36] S. Lee, S. C. Eom, J. S. Chang, C. Huh, G. Y. Sung, and J. H. Shin, *Optics Express* **18**, 11209 (2010).
- [37] G. S. Wiederhecker, L. Chen, A. Gondarenko, and M. Lipson, *Nature* **462**, 633 (2009).
- [38] G. S. Wiederhecker, S. Manipatruni, S. Lee, and M. Lipson, *Optics Express* **19**, 2782 (2011).
- [39] X. Lu, J. Y. Lee, S. D. Rogers, and Q. Lin, *Optics Letters* **44**, 4295 (2019).
- [40] Y. Zheng, Z. Fang, S. Liu, Y. Cheng, and X. Chen, *Physical Review Letters* **122**, 253902 (2019).
- [41] Z. Fang, N. Yao, M. Wang, J. Lin, J. Zhang, R. Wu, L. Qiao, W. Fang, T. Lu, and Y. Cheng, *International Journal of Optomechatronics* **11**, 47 (2017).
- [42] R. Dehghannasiri, H. Moradinejad, T. Fan, A. H. Hosseinnia, A. A. Eftekhari, and A. Adibi, in *2018 IEEE Photonics Conference (IPC)* (2018) pp. 1–2.
- [43] L. Ding, C. Baker, P. Senellart, A. Lemaitre, S. Ducci, G. Leo, and I. Favero, *Physical Review Letters* **105**, 263903 (2010).
- [44] A. Polman, *Journal of Applied Physics* **82**, 1 (1997).
- [45] B. Romeira and A. Fiore, *IEEE Journal of Quantum Electronics* **54**, 1 (2018).
- [46] J. B. Jager, P. No, E. Picard, V. Calvo, E. Delamadeleine, and E. Hadji, *Physica E: Low-dimensional Systems and Nanostructures* **41**, 1127 (2009).
- [47] H.-S. Hsu, C. Cai, and A. M. Armani, *Optics Express* **17**, 23265 (2009).
- [48] R. Perahia, J. D. Cohen, S. Meenehan, T. P. M. Alegre, and O. Painter, *Applied Physics Letters* **97**, 191112 (2010).
- [49] L. He, c. K. Özdemir, and L. Yang, *Laser & Photonics Reviews* **7**, 60 (2013).
- [50] T. J. Collins, *BioTechniques* **43**, S25 (2007).
- [51] G. N. van den Hoven, E. Snoeks, A. Polman, C. van Dam, J. W. M. van Uffelen, and M. K. Smit, *Journal of Applied Physics* **79**, 1258 (1996).
- [52] M. Pollnau, E. Heumann, and G. Huber, *Applied Physics A* **54**, 404 (1992).
- [53] E. Snoeks, G. N. v. d. Hoven, A. Polman, B. Hendriksen, M. B. J. Diemeer, and F. Priolo, *Journal of the Optical Society of America B* **12**, 1468 (1995).
- [54] J. C. Johnson, S.-M. Ku, H. V. Lillja, and P. E. Shih-To, “Method of ion implantation through a photoresist mask,” (1975), library Catalog: Google Patents.
- [55] P. G. Kik and A. Polman, *Journal of Applied Physics* **93**, 5008 (2003).
- [56] T. J. Johnson, M. Borselli, and O. Painter, *Opt. Express* **14**, 817 (2006).
- [57] C. Baker, S. Stapfner, D. Parrain, S. Ducci, G. Leo, E. M. Weig, and I. Favero, *Optics Express* **20**, 29076 (2012).
- [58] S. Diallo, G. Lin, and Y. K. Chembo, *Optics Letters* **40**, 3834 (2015).
- [59] M. Rowley, B. Wetzell, L. D. Lauro, J. S. T. Gongora, H. Bao, J. Silver, L. D. Bino, P. D. Haye, M. Peccianti, and A. Pasquazi, *Optics Express* **27**, 19242 (2019).
- [60] Y.-S. Park and H. Wang, *Optics Letters* **32**, 3104 (2007).
- [61] Because in this regime the thermo-optic effect is in the same direction as the radiation pressure forcing, it is out-competed and does not contribute to the self-pulsing in this case.
- [62] Y. Deng, F. Liu, Z. C. Leseman, and M. Hossein-Zadeh, *Optics Express* **21**, 4653 (2013).
- [63] C. Bekker, R. Kalra, C. Baker, and W. P. Bowen, *Optica* **4**, 1196 (2017).
- [64] V. R. Almeida and M. Lipson, *Optics Letters* **29**, 2387 (2004).
- [65] D. Parrain, C. Baker, G. Wang, B. Guha, E. G. Santos, A. Lemaitre, P. Senellart, G. Leo, S. Ducci, and I. Favero, *Optics Express* **23**, 19656 (2015).
- [66] D. W. Vernooy, V. S. Ilchenko, H. Mabuchi, E. W. Streed, and H. J. Kimble, *Optics Letters* **23**, 247 (1998).
- [67] H. Gao, Y. Jiang, Y. Cui, L. Zhang, J. Jia, and L. Jiang,

Journal of Lightwave Technology **36**, 5881 (2018).

[68] This is approximately linear for small changes in refractive index and is simulated using the correct parameters

for our geometry, not taking into account stress-induced warping.